JGR Atmospheres

RESEARCH ARTICLE
10.1029/2022JD037050

Abrupt Change in the Lower Thermospheric Mean Meridional Circulation During Sudden Stratospheric Warmings and Its Impact on Trace Species

Yvan J. Orsolini[1,2], Jiarong Zhang[3], and Varavut Limpasuvan[3]

[1]NILU - Norwegian Institute for Air Research, Kjeller, Norway, [2]Norwegian University of Science and Technology, Trondheim, Norway, [3]School of the Coastal Environment, Coastal Carolina University, Conway, SC, USA

Key Points:

- The lower thermospheric mean meridional circulation (MMC) reverses for about 10 days following the onset of elevated stratopause events in the northern hemisphere
- The reversals of the lower thermospheric MMC are driven by westward-propagating planetary waves
- The attendant descent leads to a enhancement of nitric oxide into the polar upper mesosphere, exceeding 1 ppm at 110 km

Correspondence to:
Y. J. Orsolini,
yvan.orsolini@nilu.no

Citation:
Orsolini, Y. J., Zhang, J., & Limpasuvan, V. (2022). Abrupt change in the lower thermospheric mean meridional circulation during sudden stratospheric warmings and its impact on trace species. *Journal of Geophysical Research: Atmospheres*, *127*, e2022JD037050. https://doi.org/10.1029/2022JD037050

Received 1 MAY 2022
Accepted 8 OCT 2022

Author Contributions:
Conceptualization: Yvan J. Orsolini, Jiarong Zhang, Varavut Limpasuvan
Data curation: Jiarong Zhang
Formal analysis: Yvan J. Orsolini, Varavut Limpasuvan
Funding acquisition: Varavut Limpasuvan
Investigation: Yvan J. Orsolini, Jiarong Zhang, Varavut Limpasuvan
Methodology: Yvan J. Orsolini, Jiarong Zhang, Varavut Limpasuvan
Resources: Varavut Limpasuvan
Software: Jiarong Zhang
Supervision: Yvan J. Orsolini, Varavut Limpasuvan
Validation: Yvan J. Orsolini, Jiarong Zhang
Visualization: Jiarong Zhang

Abstract Based on the hourly output from the 2000–2014 simulations of the National Center for Atmospheric Research's vertically extended version of the Whole Atmosphere Community Climate Model in specified dynamics configuration, we examine the roles of planetary waves (PWs), gravity waves, and atmospheric tides in driving the mean meridional circulation (MMC) in the lower thermosphere (LT) and its response to the sudden stratospheric warming phenomenon with an elevated stratopause in the northern hemisphere. Sandwiched between the two summer-to-winter overturning circulations in the mesosphere and the upper thermosphere, the climatological LT MMC is a narrow gyre that is characterized by upwelling in the middle winter latitudes, equatorward flow near 120 km, and downwelling in the middle and high summer latitudes. Following the onset of the sudden stratospheric warmings, this gyre reverses its climatological direction, resulting in a "chimney-like" feature of un-interrupted polar descent from the altitude of 150 km down to the upper mesosphere. This reversal is driven by the westward-propagating PWs, which exert a brief but significant westward forcing between 70 and 125 km, exceeding gravity wave and tidal forcings in that altitude range. The attendant polar descent potentially leads to a short-lived enhanced transport of nitric oxide into the mesosphere (with excess in the order of 1 parts per million), while carbon dioxide is decreased.

1. Introduction

Our understanding of the vertical coupling between the lower atmosphere and the upper atmosphere has significantly advanced in recent years, spurred by the large amount of new space-borne and ground-based observations and the extension of atmospheric models into the mesosphere and thermosphere. Observational and model studies have revealed that the mesosphere-lower thermosphere (MLT) region is the nexus where the forcings by gravity waves (GWs), atmospheric tides, and planetary waves (PWs) contribute to driving the mean meridional circulation (MMC). It is widely recognized that the breaking of GWs propagating from below drives a mesospheric pole-to-pole MMC with ascent at the summer pole and descent at the winter pole. Aloft, in the lower thermosphere (LT), the MMC reverses with ascent in the winter mid-to-high latitudes and descent in the summer high latitudes, accompanied by a winter-to-summer meridional flow. This narrow LT MMC was first pointed out in Liu (2007) using the TIME-GCM model and was soon after diagnosed in satellite observations of water vapor by the Sub-Millimeter Radiometer (SMR) instrument (Lossow et al., 2009) and, more recently, of carbon dioxide (CO_2) by the Sounding of the Atmosphere using the Broadband Emission Radiometry (SABER) instrument (Qian et al., 2017; Wang et al., 2022). It was later diagnosed in Whole-Atmosphere Community Climate Model (WACCM) free-running simulations by Lossow et al. (2009), Smith et al. (2011), and more recently by Qian and Yue (2017) using WACCM in specified dynamics configuration (SD-WACCM). These WACCM-based studies found that this narrow LT MMC extends approximately from 1×10^{-3} to 0.8×10^{-4} hPa (approximately 95–110 km), in broad agreement with observations. The latter study also described schematically how the LT MMC could be driven in the northern hemisphere by the breaking above the mesopause of high-phase-speed eastward-propagating GWs whose vertical propagation is unimpeded by the stratospheric eastward flow (see their Figure 1).

Higher in the thermosphere, this LT circulation transitions toward the deep summer-to-winter thermospheric MMC driven by solar heating (e.g., Forbes, 2007). Within the high latitudes of the thermosphere, auroral heating can likewise lead to a confined circulation opposing the latter.

Writing – original draft: Yvan J. Orsolini
Writing – review & editing: Jiarong Zhang, Varavut Limpasuvan

Despite having mean velocities much smaller than local tidal winds which dominate wind variability at this altitude range, the LT MMC is important for the transport of trace species, both latitudinally and vertically between the mesosphere and the thermosphere (Liu, 2007; Qian et al., 2017). Changes in the distribution of the atomic oxygen-to-molecular nitrogen (O/N_2) ratio brought about by the LT MMC variability can diffuse throughout the entire thermosphere altering its composition (Oberheide et al., 2020; Qian & Yue, 2017; Yue & Wang, 2014).

In recent years, considerable interest has arisen in the northern hemispheric sudden stratospheric warming phenomenon whose onset is followed by the reformation of an elevated stratopause at mesospheric altitudes (hereafter, ES-SSW). Since the initial discovery in the Microwave Limb Sounder (MLS) observations by Manney et al. (2008, 2009), ES-SSW events and their impact on trace species have been confirmed in other satellite datasets such as SABER (Smith et al., 2009; Tweedy et al., 2013), SMR (Orsolini et al., 2010; Pérot & Orsolini, 2021), Michelson Interferometer for Passive Atmospheric Sounding (MIPAS) (Damiani et al., 2014; Funke et al., 2010; García-Comas et al., 2020), and Solar Occultation For Ice Experiment (SOFIE) (Siskind et al., 2021). ES-SSWs have also been extensively examined using WACCM (Chandran et al., 2013, 2014; Harvey et al., 2021; Holt et al., 2013; Limpasuvan et al., 2012, 2016; Orsolini et al., 2017; Pedatella et al., 2014; Siskind et al., 2015; Tweedy et al., 2013) or the thermosphere and ionosphere extension of WACCM (i.e., WACCM-X) (Oberheide et al., 2020; Sassi et al., 2013; Siskind et al., 2021; Zhang et al., 2021), in free-running, specified dynamics, or data assimilation configurations. Other model studies of ES-SSWs include those based on the TIME-GCM model in specified dynamics configurations (Jones et al., 2020), the Ground-to-topside model of Atmosphere and Ionosphere for Aeronomy (GAIA) model (Liu et al., 2014; Miyoshi et al., 2015) or GW-permitting high-resolution middle atmosphere general circulation models (Okui et al., 2021; Tomikawa et al., 2012). Finally, high-altitude re-analyses from the U.S. Navy NAVGEM system have also been used to study the dynamical evolution of ES-SSWs (Laskar et al., 2019). An extensive review of the impacts of sudden stratospheric warming events (in practice, of ES-SSWs) on the upper atmosphere is recently provided by Goncharenko et al. (2021).

The modeled ES-SSW events exhibit the unanticipated appearance of westward-traveling PWs (hereafter, WPWs) with zonal wavenumbers 1–2 due to the in situ instability of the reversed polar upper stratospheric wind (Limpasuvan et al., 2016; Tomikawa et al., 2012). With periods between 5 and 12 days, WPWs generated after the ES-SSW onset propagate upward into the MLT, where their existence has been confirmed by observations from the SuperDARN radar network near 95 km (Stray et al., 2015) and by SABER temperature observations (e.g., Chandran et al., 2013; Orsolini et al., 2017). Eastward-propagating PWs (hereafter, EPWs) are also prevalent in the upper mesosphere (Iwao & Hirooka, 2021). They have been observed to become enhanced in the weeks prior to the onset of ES-SSWs in case studies using MLS observations (Iida et al., 2014) or the WACCM model (Rhodes et al., 2021). The ES-SSW events further elicit a tidal response with both models and observations pointing to the enhancement of the semi-diurnal migrating tide (SW2) as well as other non-migrating semi-diurnal tides and quasi-tidal perturbations (with periods close but not exactly equal to 12 hr) in the weeks following onset (Conte et al., 2019; Goncharenko et al., 2012; Hibbins et al., 2019; Jin et al., 2012; Limpasuvan et al., 2016; Orsolini et al., 2017; Pedatella et al., 2014; Sassi et al., 2013, 2021; Zhang et al., 2021).

With the onset of ES-SSW, the anomalous westward stratospheric zonal-mean winds selectively allow eastward GWs into the mesosphere. The subsequent breaking of these GWs imposes an anomalous eastward GW drag (GWD) that would induce upwelling in the polar mesosphere and potentially augment to upwelling associated with the LT MMC. However, based on SD-WACCM, Limpasuvan et al. (2016) and Orsolini et al. (2017) demonstrated that WPW driving can offset this anomalous eastward GWD in the LT for a short period (~14 days) after the ES-SSW onset, leading instead to enhanced polar descent. Orsolini et al. (2017) also found that WPWs contribute much more to the wave driving in the northern hemisphere mid and high latitudes in the 90–130 km layer than migrating tides. Furthermore, based on free-running case study simulations using the GAIA and WACCM-X models, Miyoshi et al. (2015) and Oberheide et al. (2020), respectively, suggested that LT MMC briefly reversed. However, the robustness of such changes in the LT MMC and the dominant wave forcings involved remain unclear. Thus, despite the suggested role of fast eastward GWs above the mesopause in driving the climatological LT MMC (Qian & Yue, 2017) and the general importance of tidal dissipation in driving the overall thermospheric MMC (Jones et al., 2020), the anomalous WPW forcings induced during ES-SSWs may strongly impact the LT MMC. The relative influences of various wave forcings on the LT MMC and its subseasonal variability are still poorly understood.

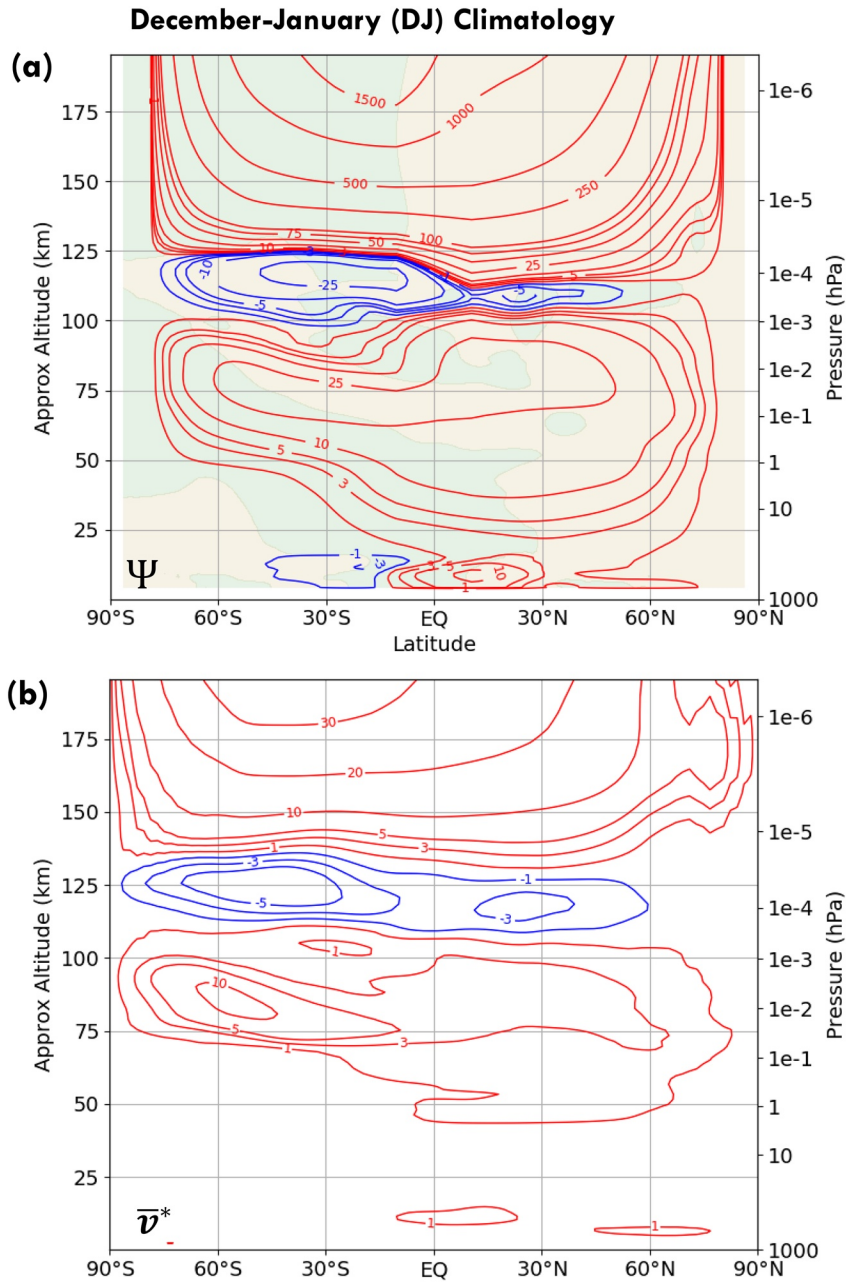

Figure 1. *Wintertime climatological meridional cross-sections of the residual mean meridional circulation* (*MMC*). Altitude-meridional cross-sections of velocity streamfunction (a) and meridional component (b) of the residual MMC. Red (blue) contours show clockwise (counterclockwise) circulation. Filled regions indicate vertical component with green (orange) indicates positive (negative) values. Labels are indicated on contours. The climatology is based on December and January, in quiet winters without ES-SSW events. The units are 10^{-4} m/s and m/s, respectively.

To this end, the present paper examines the composite LT MMC and its variability during ES-SSWs to clarify the respective roles of PWs, tides and GWs. In using WACCM-X that extends above 500 km and nudged by observations below the stratopause, our examination avoids the vertical limitation that may influence the LT region, as was the case for the aforementioned WACCM results, while still tied to the observed ES-SSW events. We find that, during ES-SSW, the composite LT MMC abruptly reverses its climatological direction due to WPW forcing which exert a brief but significant westward forcing between 70 and 125 km, exceeding GWD and tidal forcings in that altitude range. The circulation reversal favors an uninterrupted polar descent from the altitude of 150 km down to the upper mesosphere, resulting in a short-lived enhanced transport of nitric oxide (NO) into the

mesosphere. To our knowledge, deciphering the robust wave forcing responsible for this remarkable LT MMC reversal during ES-SSWs has not been documented before.

2. Model Description and Methods

With a top boundary between 500 and 700 km (depending on the solar and geomagnetic activity), WACCM-X incorporates processes needed to resolve the thermosphere energetics and thermal structure, but also includes representations of the lower atmospheric physical processes found in WACCM (Marsh et al., 2013). WACCM-X V2.0 (Liu et al., 2018) has been recently used to study diverse upper-atmosphere and ionosphere phenomena ranging from climate change (Solomon et al., 2018) to solar eclipse effects (McInerney et al., 2018). The simulated tides are stronger in WACCM-X than in WACCM due to a lesser damping of the divergent flow (Liu et al., 2018).

Simulations with the WACCM-X V2.0 in specified dynamics configuration (hereafter, referred to as SD-WACCM-X) covering the period 2000–2014 with hourly output were released as part of the National Center for Atmospheric Research (NCAR) Community Earth System Model version 2. With the hourly output, we can analyze the semi-diurnal tide in addition to the diurnal tide. The tides are extracted by a 2D Fourier transform in longitude and time that can separate the migrating and non-migrating components (see details in Zhang et al., 2021). The semi-diurnal tide hereafter comprises periods between 11.8 and 12.2 hr and the diurnal tide periods between 23.8 and 24.2 hr. While dynamical output is archived hourly, the abundance of CO_2 and NO is only archived as a daily average in version V2.0.

In this configuration, the model temperature, surface pressure, and wind fields are constrained below 50 km by NASA Modern-Era Retrospective Analysis for Research and Application (MERRA-2) (Gelaro et al., 2017). Above 60 km, the model is fully interactive and free running. The horizonal resolution is 1.9° latitude by 2.5° longitude. In these simulations, the zonal phase speeds prescribed in the parametrization of GWs due to frontogenesis range from +80 to −80 m s^{-1}.

To elucidate wave activity, we compute the residual MMC based on the Transformed Eulerian Mean (TEM) formulation in log-pressure vertical coordinates (Andrews et al., 1987) using hourly data, as well as the Eliassen-Palm (EP) flux and its divergence (EPFD). In the following, the daily mean EPFD due to PWs includes traveling waves with zonal wavenumbers 1–5 and periods between 2 and 20 days and is partitioned in contributions from WPWs and EPWs. The daily mean EPFDs due to the main tides (in particular the migrating DW1 and SW2) are also calculated, following Zhang et al. (2021). The EPFD will be compared to the GWD from parametrized GWs, which account for wave sources due to fronts, orography, and convection.

The velocity streamfunction $\Psi(t, \phi, z)$ of the residual mean circulation can be estimated from a latitudinal integration of the vertical component of the residual mean flow ($\overline{w}^*$) with a boundary condition of $\Psi = 0$ at the North Pole or the South Pole.

$$\Psi(t, \phi, z) = -\int_{\phi}^{\frac{\pi}{2}} \cos\ \phi_0 \overline{w}^* \, d\phi_0 \text{ for Northern Hemisphere} \quad (1)$$

$$\Psi(t, \phi, z) = \int_{-\frac{\pi}{2}}^{\phi} \cos\ \phi_0 \overline{w}^* \, d\phi_0 \text{ for Southern Hemisphere} \quad (2)$$

where t, ϕ, z represent time, latitude and altitude. The unit of Ψ is m s^{-1}.

The contributions of the different wave forcings to the velocity streamfunction are estimated from the method of Sato and Hirano (2019), based on the downward-control principle. Thus, $\Psi(t, \phi, z)$ is expressed as a sum of four components:

$$\Psi(t, \phi, z) = \Psi_{RW}(t, \phi, z) + \Psi_{GW}(t, \phi, z) + \Psi_X(t, \phi, z) + \Psi_{tend}(t, \phi, z) \quad (3)$$

representing contributions by resolved waves (RW), parameterized gravity waves (GW), friction and viscosity term (X), and the zonal wind tendency (tend):

$$\Psi_{\mathrm{RW}}(t,\phi,z) = -\frac{1}{\rho_0 a}\int_z^{\infty}\left[\frac{\nabla\cdot\boldsymbol{F}}{a\hat{f}}\right]_{\overline{m}}\mathrm{d}z_0 \tag{4}$$

$$\Psi_{\mathrm{GW}}(t,\phi,z) = -\frac{\cos\phi}{\rho_0 a}\int_z^{\infty}\left[\frac{\rho_0}{\hat{f}}\overline{\mathbf{GWD}}\right]_{\overline{m}}\mathrm{d}z_0 \tag{5}$$

$$\Psi_{\mathrm{tend}}(t,\phi,z) = \frac{\cos\phi}{\rho_0 a}\int_z^{\infty}\left[\frac{\rho_0}{\hat{f}}\frac{\partial\overline{u}}{\partial t}\right]_{\overline{m}}\mathrm{d}z_0 \tag{6}$$

Here $\boldsymbol{F}$ is the EP flux due to RWs, $\overline{\mathbf{GWD}}$ is the gravity wave drag, ρ_0 is density, a is the earth radius, $\overline{m} = a\cos\phi\left(\overline{u} + a\Omega\cos\phi\right)$ is the zonal mean angular momentum per unit mass, and $\hat{f} = 2\Omega\sin\phi - \frac{1}{a\cos\phi}\frac{\partial(\overline{u}\cos\phi)}{\partial\phi}$. The integral represents a vertical integration along a constant $\overline{m}$. Ψ_{X} is estimated as the residual between Equations 1 and 3.

Ψ_{RW} can be further decomposed by using the different wave components of the EPFD, such as SW2, DW1, WPWs, and EPWs. The streamfunction is calculated from daily means or from the composited or climatological residual velocities using Equations 1 and 2, but we verified that integration from hourly data provides a very similar, albeit slightly noisier, result.

We identify and composite 9 ES-SSW events in SD-WACCM-X over the 2000–2014 period, occurring between December and January. The ES-SSW onset dates are taken from Limpasuvan et al. (2016) based on SD-WACCM and are: 10 December 2000, 22 December 2001, 29 January 2001, 19 December 2003, 8 January 2006, 21 January 2009, 22 January 2010, 13 January 2012, and 5 January 2013. Criteria from Limpasuvan et al. (2016) identify an ES-SSW occurrence based on a zonal average between 70 and 90°N if (a) the temperature falls below 190 K between 80 and 100 km, (b) the zonal-mean zonal wind reverses to westward at 1 hPa and persists longer than 5 days, and (c) the stratopause altitude based on the zonal-mean temperature maximum between 20 and 100 km exhibits a vertical discontinuity of at least 10 km. Before compositing, each SSW event is aligned with respect to its onset date (defined to be day 0) during which the polar cap (70–90°N) zonal-mean zonal wind reversal occurred at 1 hPa. A quiet winter climatology, characterized by the circulation without ES-SSW events, is constructed using the remaining 6 winters from the 2000–2014 period.

We note that figures showing the pressure distribution of various diagnostics are accompanied, along the ordinates, with the approximate altitude levels converted from the model's isobaric levels using log-pressure coordinates formulation which depends on the standard scale height. Gravity and the gas constant for dry air used to compute the standard scale height are allowed to vary with pressure levels above 10^{-2} hPa, based on the U.S. Standard Atmosphere 1975, as in Zhang et al. (2021). As such, the shown approximate altitudes will be slightly different than those in Qian et al. (2017).

3. Results

3.1. The Climatological Mean Meridional Circulations

We begin by showing the climatological structure of the three MMC cells across the stratosphere, the mesosphere and the LT in SD-WACCM-X, based on the quiet winters defined above. Figure 1 shows the altitude-latitude cross-sections from the surface to 200 km of the climatological (i.e., quiet winter) MMC as represented by the velocity streamfunction (Figure 1a) and the meridional component of the residual mean flow ($\overline{\boldsymbol{v}}^*$ in Figure 1b). A narrow counterclockwise circulation, the LT MMC illustrated in the velocity streamfunction as blue contours in Figure 1a), spans the layer 100–125 km, above the familiar clockwise mesospheric MMC which is characterized by high-latitude ascent in the summer hemisphere, poleward motions and descent maximizing above the winter polar stratopause. Bounded above by the thermospheric summer-to-winter MMC, this narrow LT MMC is characterized by weak ascent near 105–115 km at middle to subpolar latitudes (30–60°N) and by southward motions

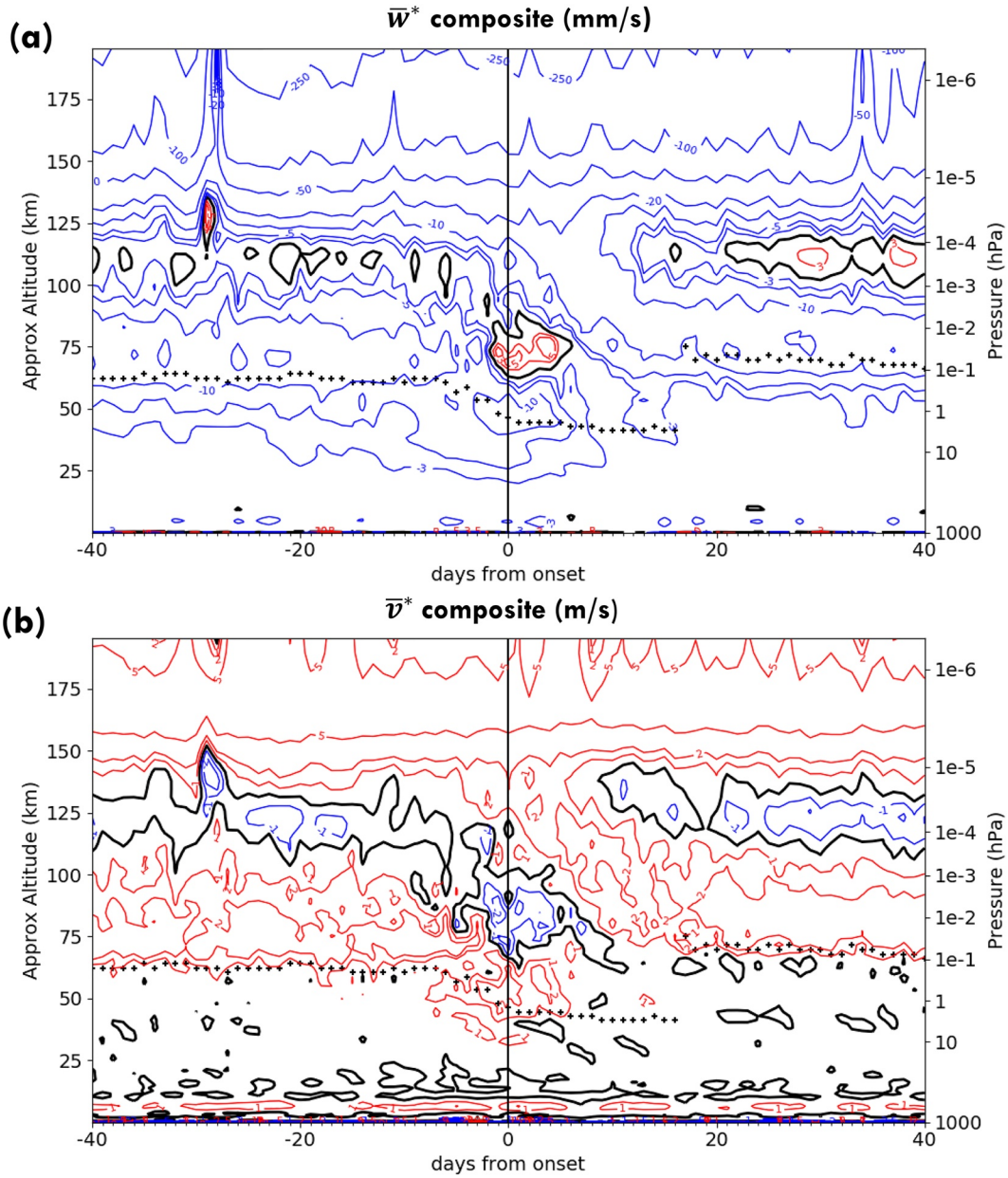

Figure 2. *Composite residual mean meridional circulation* (*MMC*). Altitude-time cross-sections of the vertical (a) and meridional (b) components of the residual MMC composite of 9 ES-SSW events from the 40 days prior to 40 days after the onset. A latitude averaging over 62–79°N was done. Red contours show the positive velocities, blue contours show the negative velocities, and the thick black contours indicate zero velocity. The units of vertical and meridional components are mm/s and m/s, respectively. The line dotted with stars indicates the stratopause.

that extend to the summer pole. In the southern hemisphere, the LT MMC is thicker, and the associated $\overline{v}^*$ peaks at slightly higher altitude (by ∼8 km).

3.2. The Perturbed Mean Meridional Circulations During ES-SSWs

Focusing now on the winters characterized by ES-SSW events, we first display the time evolution of the components of the MMC around the onset. Figure 2 shows the altitude-time cross-sections of the ES-SSW composited $\overline{w}^*$ and $\overline{v}^*$ (averaged 62–79°N) from 40 days prior to 40 days after the onset. Prior to the onset (days [−40, −5]) and after the onset (days [20, 40]), one can identify the narrow LT circulation extending up to 130 km, with weak

ascent maximizing near 115 km and equatorward flow maximizing near 125 km, similar to the climatology in Figure 1. For a brief period of around 10 days, starting a few days prior to the onset, there is ascent and equatorward motions in the mesosphere, approximately between 60 and 90 km. This mesospheric reversal has been described extensively in the studies mentioned in Section 1. Higher up, there is however a marked contemporaneous reversal of the LT circulation, until about 10–14 days after the onset when both $\overline{v}^*$ and $\overline{w}^*$ revert to their respective climatological directions. During the intermediary period, roughly between days 5 and 15, the uninterrupted descent (negative $\overline{w}^*$) from the thermosphere to the upper stratosphere characterizes a "polar chimney."

In Figure 2, we also note the anomalously strong but short-lived ascent (accompanied by an enhanced equatorward flow) around day −30 and near 125 km in the composites. These features mostly originate from the ES-SSW 2003 event and are linked to auroral heating following the "Halloween" geomagnetic storms in October 2003–November 2003. These anomalies are inconsequential for the rest of this study, which focuses on the period following onset.

We now consider the meridional extent of the overall MMC changes including those in the LT MMC, shortly after the ES-SSW onset. The left column of Figure 3 shows the altitude-latitude cross-sections of the anomalous zonal-mean temperature (Figure 3a), velocity streamfunction (Figure 3b), and $\overline{v}^*$ (Figure 3c) composited over days [5, 15]. The right column shows the corresponding composite of the total fields (Figures 3d–3f). Between approximately 95 and 125 km, there is layer of anomalous poleward motions (Figure 3c) associated with anomalous descent (Figure 3b) and warming (Figure 3a) from the mid-latitudes (about 40°N) to the North Pole. Near the top of this layer around 125 km, the poleward motions in fact begin further south, in the summer subtropics where ascent also prevails. Below, between around 70 and 90 km, there is an anomalous equatorward return branch that extends from the North Pole to the summer subtropics. It is situated atop the mesospheric MMC cell, providing by continuity equatorward motions at the level where the polar mesospheric ascent stops. The anomalous poleward $\overline{v}^*$ at 125 km is sufficiently large to alter the direction of the total $\overline{v}^*$. Indeed, Figure 3f reveals that the total $\overline{v}^*$ is northward at latitudes poleward of 45°N, in contrast to the climatological $\overline{v}^*$ in Figure 1b. This brief reversal agrees well with the free-running case-study using WACCM-X in Oberheide et al. (2020). Our study is also broadly consistent with the GAIA model results in Miyoshi et al. (2015), but further highlights that both the LT MMC and the mesospheric circulation act together for a brief period of time to induce downward motions.

Between 150 and 200 km, the influence of ES-SSWs expands globally, with an anomalous southward flow intensifying in the southern hemisphere, opposing the background thermospheric MMC (Figure 3c). At the same time, temperature anomalies are positive, albeit not significant (Figure 3a).

3.3. The Wave Drivers of the Perturbed Mean Meridional Circulations

To get insight into the dominant wave forcings of the zonal-mean flow around the onset, we initially decompose the total wave forcing into the contributions from the parametrized total GWD and the EPFD associated with WPWs and EPWs as altitude-time cross-sections (Figures 4a–4c, respectively). A latitude averaging has been performed over 40–80°N, as well as a daily mean. The large, transient WPW forcing appears between 75 and 125 km and overlaps with the period of reversed (eastward) GWD. This overlapping commences a few days prior to onset and persists to about day 10. During that period, the GWD is uniformly eastward at all altitudes below 125 km while, prior to the onset, it was predominantly eastward higher in the 100–130 km range. Eastward acceleration by EPWs generally appears in a narrow layer centered around 75 km (Figure 4c). Just before the ES-SSW onset, the enhanced EPW forcing is indicative of EPW emission by shear instability reported by Iida et al. (2014), Iwao and Hirooka (2021), and Rhodes et al. (2021). However, in the layer where the LT MMC prevails in the northern hemisphere, the GWD typically provides the main eastward forcing contribution.

We next further compare the relative magnitudes of these GWs, PWs, and tidal wave forcings across the three altitude ranges that are representative of the mesospheric, the LT and the thermospheric MMCs. Figure 5 details the zonal-mean flow forcing contributions over 70–95 km (Figure 5a), 115–135 km (Figure 5b), and 120–200 km (Figure 5c). Averaged over 40–80°N, the forcings can be either westward (designated by the letter W in the ordinate label) or eastward (designated by the letter E). Figure 5b clearly reveals that the LT MMC, prior to or after the ES-SSW, is driven by the eastward GWD (red line) which comprise most of the total forcing (black line). Appendix A further details the contributions of frontal GWs of different phase speeds in a different set of

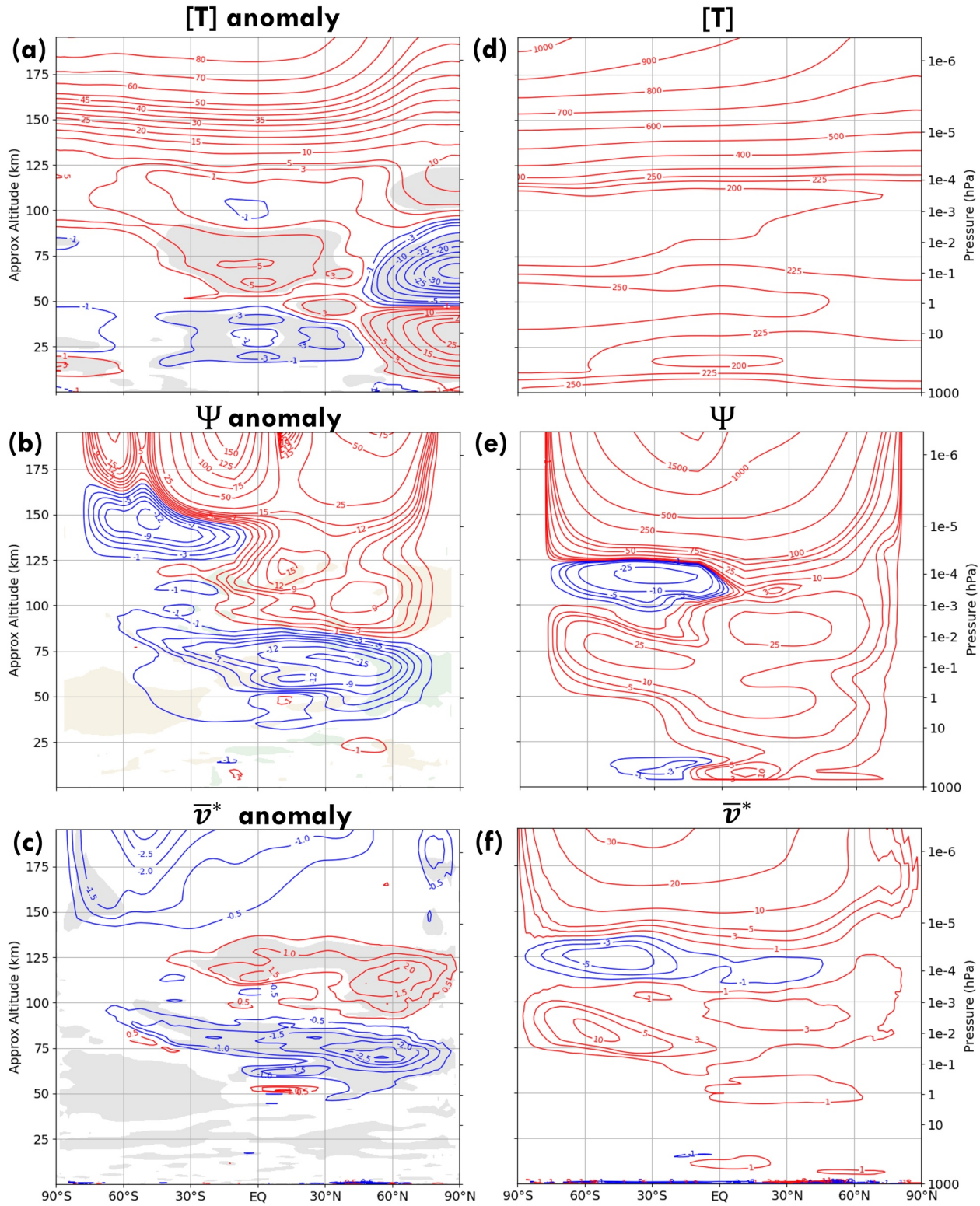

Figure 3. *Meridional cross-sections of temperature and residual mean meridional circulation (MMC) after onset.* Altitude-meridional cross-sections of zonal-mean temperature anomalies (a), anomalous velocity streamfunction (b), and anomalous meridional component of the residual MMC (c). The anomalies are composited from 9 ES-SSW events and averaged over days [5, 15] after onset. Red (blue) contours show positive (negative) anomalies. Labels are indicated on contours. Gray filled regions in panels (a and c) indicate where the *t*-test statistical significance level is above 95%. In panel (b), green (orange) filled region indicates anomalous positive (negative) vertical component of the residual MMC is significant. The total composited for the same variables are shown in right column (d–f). The units are K, 10^{-4} m/s and m/s, respectively.

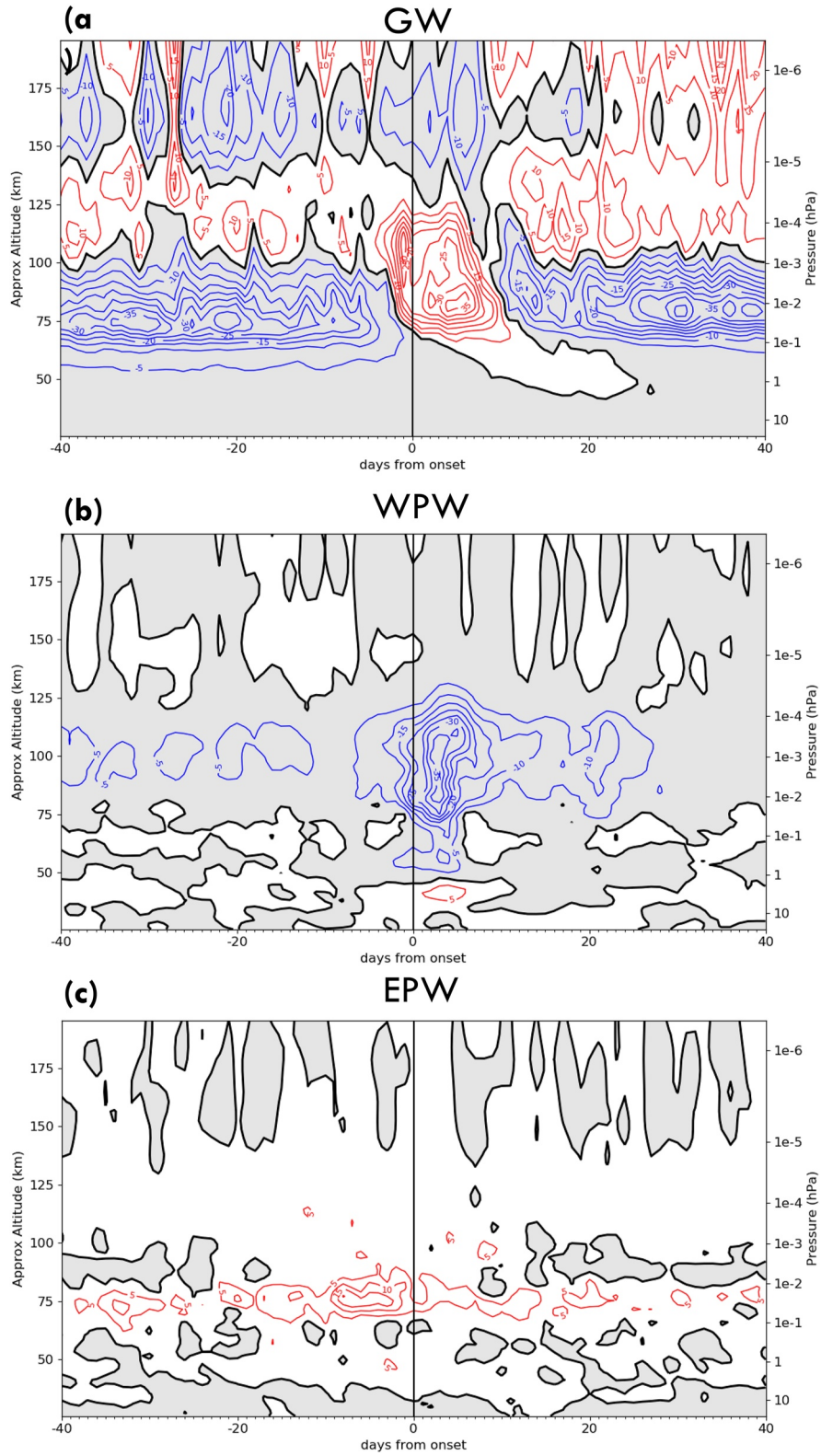

Figure 4. *Composite wave forcings*. Altitude-time cross-sections of the total parametrized gravity wave (GW) drag (including frontal, orographic, and convective GWs) (a), of westward-propagating planetary waves (PWs) forcing (wavenumbers 1–5) (b), and of eastward-propagating PWs forcing (wavenumbers 1–5) (c) composited from 9 ES-SSW events during the 40 days prior to 40 days after the onset. A latitude averaging over 40–80°N was done. Red contours show eastward values, blue contours show westward values, and the thick black contours indicate the zero value. Units are m/s per day.

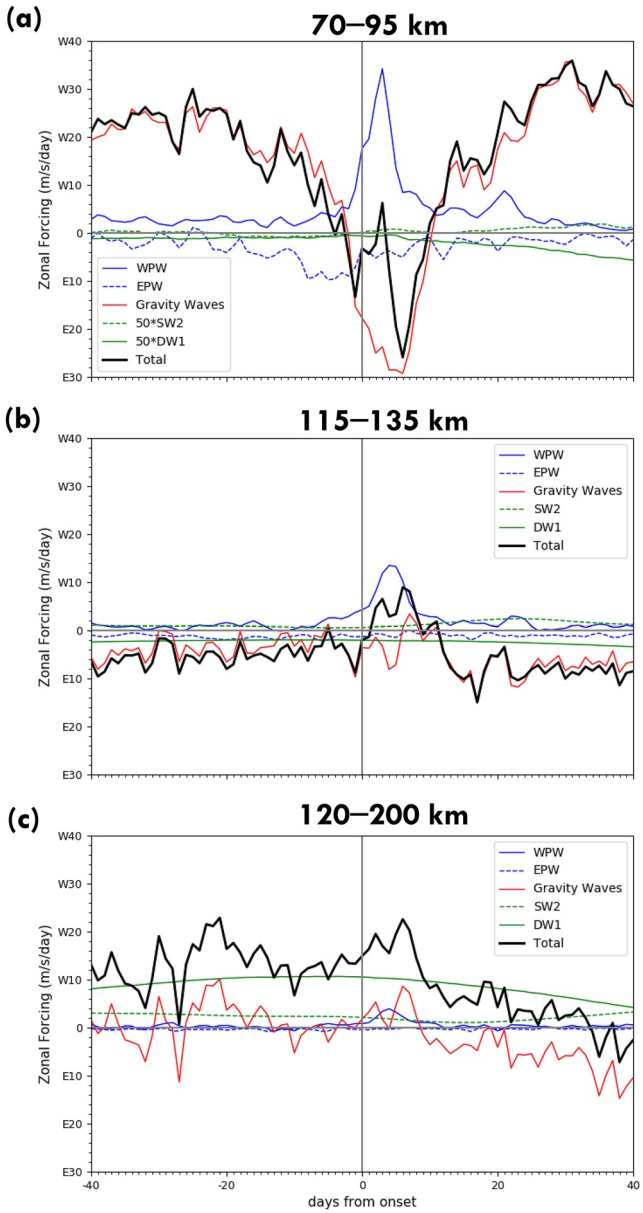

Figure 5. *Components of zonal-mean wave forcing of the mesospheric, lower thermospheric and thermospheric mean meridional circulations (MMCs).* Contributions from the westward-propagating planetary waves (PWs) (blue solid line), eastward-propagating PWs (blue dashed line), parametrized gravity wave drag (red line), semi-diurnal migrating tide (SW2, green dashed line), diurnal migrating tide (DW1, green solid line), and their total (black line). A latitude averaging over 40–80°N was done. (a) 70–95 km for the mesospheric. (b) 115–135 km for the lower thermospheric and (c) 120–200 km for the thermospheric MMCs. The contributions from tides have been multiplied by a coefficient 50 in panel (a). On *y*-axis, E or W indicate eastward and westward forcing respectively.

WACCM simulations to support the notion that fast eastward GWd drive the climatological LT MMC. Consistent with Limpasuvan et al. (2012, 2016), we see the pronounced westward forcing by WPWs (blue line) at both 70–95 km and 115–135 km layers between days 0–15 (Figures 5a and 5b). During this period, the WPW driving opposes and, at times, surpasses the eastward GWD, making the net forcing (black line) westward. On the other hand, the eastward forcing by EPWs is confined near a layer where they diverge and maximizes prior to the onset (Figure 5a). In summary, GWs normally drive the LT MMC, but WPWs play a key role immediately after the ES-SSW onset when they initiate the descent around 100 km as seen in Figure 2a.

The tidal contributions from DW1 and SW2 in this extratropical average remain small in the lower two altitude ranges. Note that their contributions are already multiplied by 50 in the lower altitude range. It is only in the upper altitude range (120–200 km) that the tidal forcings, then mainly from DW1, contribute to driving the MMC in the winter extratropics.

One can further reconstruct the contributions of the different daily mean wave forcings to the total streamfunction based on the downward-control principle, following Oberländer et al. (2013) and Sato and Hirano (2019). Since the MMC is a non-local response to the wave forcings, this principle requires a vertical integration of the wave forcings above the level where the velocity streamfunction is evaluated. Using Equation 3, we explicitly calculated the contributions of the different wave forcings (i.e., RWs such as WPWs, EPWs, and tides, as well as parametrized GWs) to the velocity streamfunction averaged over the 40–80°N latitude band at 110 km. This altitude centrally locates the LT MMC reversal as revealed in Figure 3. The contributions from the zonal-mean zonal wind tendency term and the friction and viscosity term were also calculated, the latter estimated as the residual from the total velocity streamfunction resulting from the integration of $\overline{w}^*$ (Equation 1). These various contributions to the streamfunction are shown in Figures 6a and 6b, and confirm the results from the forcing decomposition (Figure 5b), namely that WPWs overtake the GWs as the dominant forcing term for a short period after the onset. In particular, WPWs are the main contributor to the positive (clockwise) velocity streamfunction while, on the contrary, the streamfunction was negative (counter-clockwise) at long leads prior to the ES-SSW event, with the GWD is the leading contributor. At this altitude, it is interesting to note that the friction and viscosity term is not negligible, as normally found in the stratosphere.

3.4. Impact of the LT MMC Reversal on the Distribution of CO_2 and NO

The abrupt and short-lived LT MMC reversal has important implications for the transport of key trace species like CO_2 and NO. CO_2 has a long chemical lifetime but ceases to be well-mixed in the mesosphere, where it displays a strong vertical gradient (Garcia et al., 2014; Smith et al., 2011). Figure 7 shows the altitude-latitude cross-sections of the quiet winter climatology of the zonal-mean CO_2 mixing ratio (Figure 7a) and its vertical gradient (Figure 7b, blue shading). The CO_2 isopleths tighten in the high summer latitudes, with the vertical gradient maximizing near 105–110 km near the South Pole, and at slightly lower altitudes away from the pole. In the northern hemisphere, there is a "fork" of relaxed and strong gradients (near 90 and 120 km, respectively) extending from the mid-latitudes to the pole. These regions of relaxed and strong vertical gradients mark the base and the top of the LT MMC, respectively, as pointed out by Qian et al. (2017) and Wang et al. (2022) based on analysis of SABER CO_2 observations. The presence of larger gradients in the summer high latitudes in the model is in

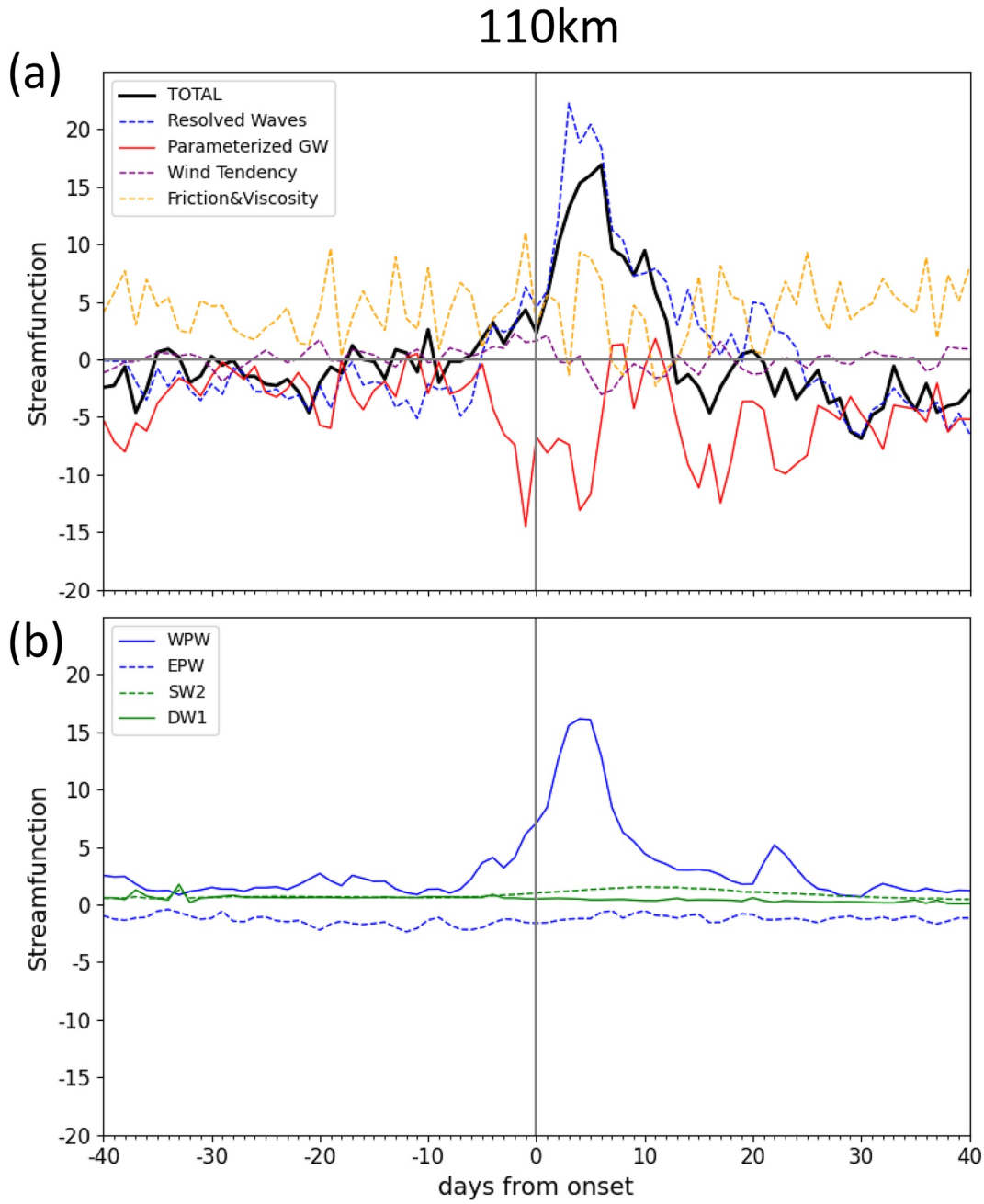

Figure 6. *Contributions to the total velocity streamfunction*. (a) Contributions to the total velocity streamfunction (black line) at 110 km by the resolved waves (dashed blue line), parametrized gravity wave drag (red line), zonal wind tendency (dashed purple line), and the residual contribution from the friction and viscosity term (dashed orange line). (b) Contributions the resolved waves by westward-propagating planetary waves (PWs) (blue solid line), eastward-propagating PWs (blue dashed line), semi-diurnal migrating tide (SW2, green dashed line) and diurnal migrating tide (DW1, green solid line). A positive velocity streamfunction indicates a clockwise circulation. A latitude averaging over 40–80°N was done. The unit is 10^{-4} m/s.

agreement with those observational studies. Following the ES-SSW onset, the composited CO_2 anomaly for days [5, 15] (Figure 7c) shows a decrease in mixing ratios at northern high latitudes that is consistent with the descent between 125 and 80 km (Figure 3b). Vertical gradients in the composite during days [5, 15] overlaid on their climatological values (Figure 7b, blue dashed lines) reveal that, following the LT MMC reversal, the layer with strong (pinched) vertical gradient in the high-latitude LT is weakened, while at northern mid-latitudes (30–60°N) between 120 and 140 km, the gradients are increased (see also CO_2 anomaly in Figure 7c).

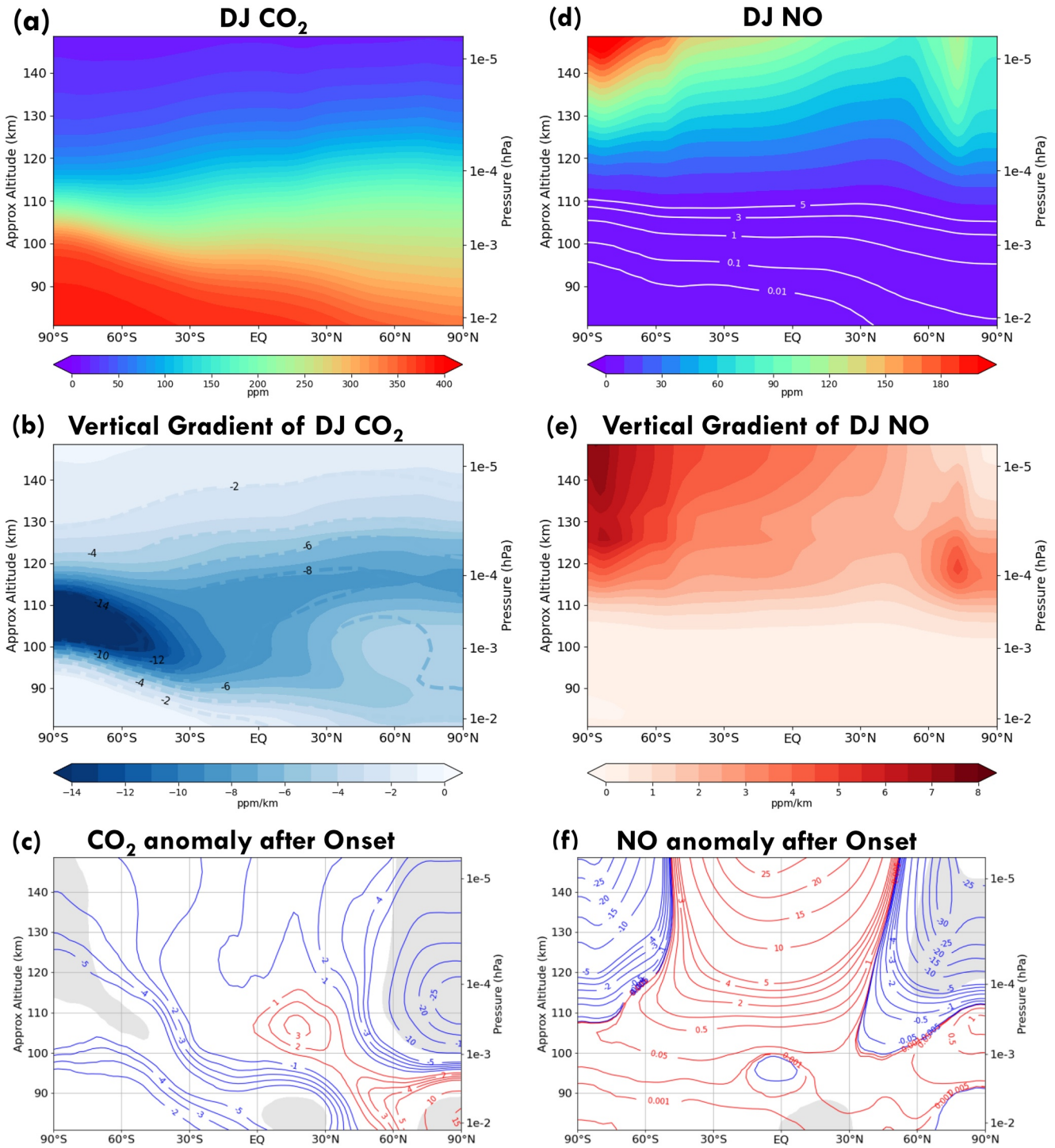

Figure 7. *Meridional cross-sections of CO_2 and NO*. Altitude-meridional cross-sections of the climatological zonal-mean CO_2 mixing ratio (a) and its vertical gradient (b). The climatology is based on December and January, excluding ES-SSW events. Anomalies of CO_2 mixing ratio composited from 9 ES-SSW events and averaged over days [5, 15] after onset are shown in panel (c), with red contours being positive anomalies and blue contours negative anomalies. Labels are indicated on contours. Gray filled region indicates where the *t*-test statistical significance level is above 95%. The vertical gradient in the composite is overlain in panel (b) as contour lines. The corresponding figures for NO are shown in (d–f). The units are ppm (a, c, d, and f) and ppm/km (b and e).

NO is another key trace species in the middle and upper atmosphere. Produced by hard solar radiation (i.e., Extreme-UV and X-Rays) and by energetic particle precipitation (EPP) at high latitudes, its abundance increases with altitude, unlike CO_2. Due to its long lifetime in darkness, NO plays a important role in the catalytic destruction

of ozone following transport into the middle atmosphere. Figure 7 (right column) shows altitude-latitude cross-sections of the corresponding climatological zonal-mean NO mixing ratio (Figure 7d) and its vertical gradient (Figure 7e). In the winter high latitudes, the upward motion associated to the climatological LT MMC hinders downward transport of NO from its lower thermospheric reservoir into the mesosphere, leaving only eddy and molecular diffusion as the irreversible processes to help NO permeate across the mesopause. The high abundance within the entire polar cap in the southern hemisphere and the narrower maximum confined near 70°N in the northern hemisphere reflect NO production by EPP along the auroral zones in the LT. The interhemispheric difference in the latitudinal extent of the high-latitude NO enhancement is due to the auroral oval being more displaced from the pole in the southern hemisphere, hence spanning a larger geographical latitude range than in the northern hemisphere where it is more zonally aligned along the 70°N parallel. With the LT MMC reversal during ES-SSW, the composite in (Figure 7f) shows a high-latitude enhancement of NO, albeit not significant, extending from 110 to 90 km and meridionally confined to higher latitudes within the northern polar cap to 60°N but extending into the upper mesosphere at lower latitudes. Peak zonally averaged values in excess of 1 ppm are found near the pole at 110 km.

The spatial extent of the NO enhancement can be gleaned from horizontal maps of the NO abundance. Figure 8 shows the climatological NO abundance at 140 km (Figure 8a), where the a-forementioned EPP production along auroral ovals dominates, and at 95 km (Figure 8c) where the NO abundance is much lower and more homogeneous. The composited anomaly maps after ES-SSW onset reveal different characteristics at these two altitudes (Figures 8b–8d). At 140 km, there is an NO reduction in a ring around 70°N consistent with the poleward motions at the edge of the production oval. However, at 95 km, there is a broad NO increase within the polar cap consistent with the enhanced descent, albeit not zonally symmetric. This local NO enhancement is up to near 0.3 ppm at 80°N.

We reiterate the main finding that the WPW activity provides the main forcing and contribution to the velocity streamfunction during the short-lived LT MMC reversal leading to the uninterrupted descent of NO from its lower thermospheric reservoir.

4. Discussion and Summary

The relative enhancement in NO can be even larger during individual ES-SSW events. As shown in Figure 9 for the 2012–2013 event also described in Orsolini et al. (2017) the zonal-mean NO enhancement of 3 ppm peaking near 110 km and 85°N corresponds to an enhancement three times higher than the composited case, due a marked descent from the LT MMC reversal following onset.

In a case study of the same 2012–2013 event, Sassi et al. (2021) showed that constraining WACCM-X dynamics with the re-analyses based on the high-altitude version of the Navy Global Environmental Model (NAVGEM-HA), which extend much higher into the mesosphere than conventional re-analyses (e.g., MERRA-2), reduced the amplitude of some traveling PWs and tides in the MLT (namely, the 2-day wave and the DE3 tide) compared to a free-running version of WACCM-X. This result raises an interesting question as to whether the amplitude of the PWs driving the descent after onset would also be reduced if WACCM-X were driven by NAVGEM-HA compared to the current simulations driven by MERRA-2, where the mesosphere is unconstrained.

Orsolini et al. (2017) showed that the largest discrepancies between SMR and the standard SD_WACCM during that 2012–10213 event were in the lower mesosphere, associated with the descending tongue of enriched NO (their Figure 3), rather than in the NO reservoir region aloft in the MLT. Using the NAVGEM-HA driven simulation, Siskind et al. (2021) illustrated that the downward transport of NO from the mesosphere into the stratosphere is in better agreement with SOFIE observations than suggested by earlier SD-WACCM simulations driven by MERRA (Orsolini et al., 2017). These authors further pointed out that subtle differences in the treatment of GWs in the re-analysis systems might be more important for constraining the NO transport and descent than the driving by the large-scale flow. However, they did not explore if the NO descent did originate above the mesopause. Orsolini et al. (2017, their Figure 7) showed that the descent during that same event, as diagnosed as very dry air in water vapor observations by SMR, initiated briely after onset above 10^{-4} hPa. The magnitude of the descent in the current SD-WACCM-X is on the order of 10–20 mm s^{-1} at 95–100 km following onset and is thus similar to the values obtained in Orsolini et al. (2017) or Limpasuvan et al. (2016) based on SD-WACCM.

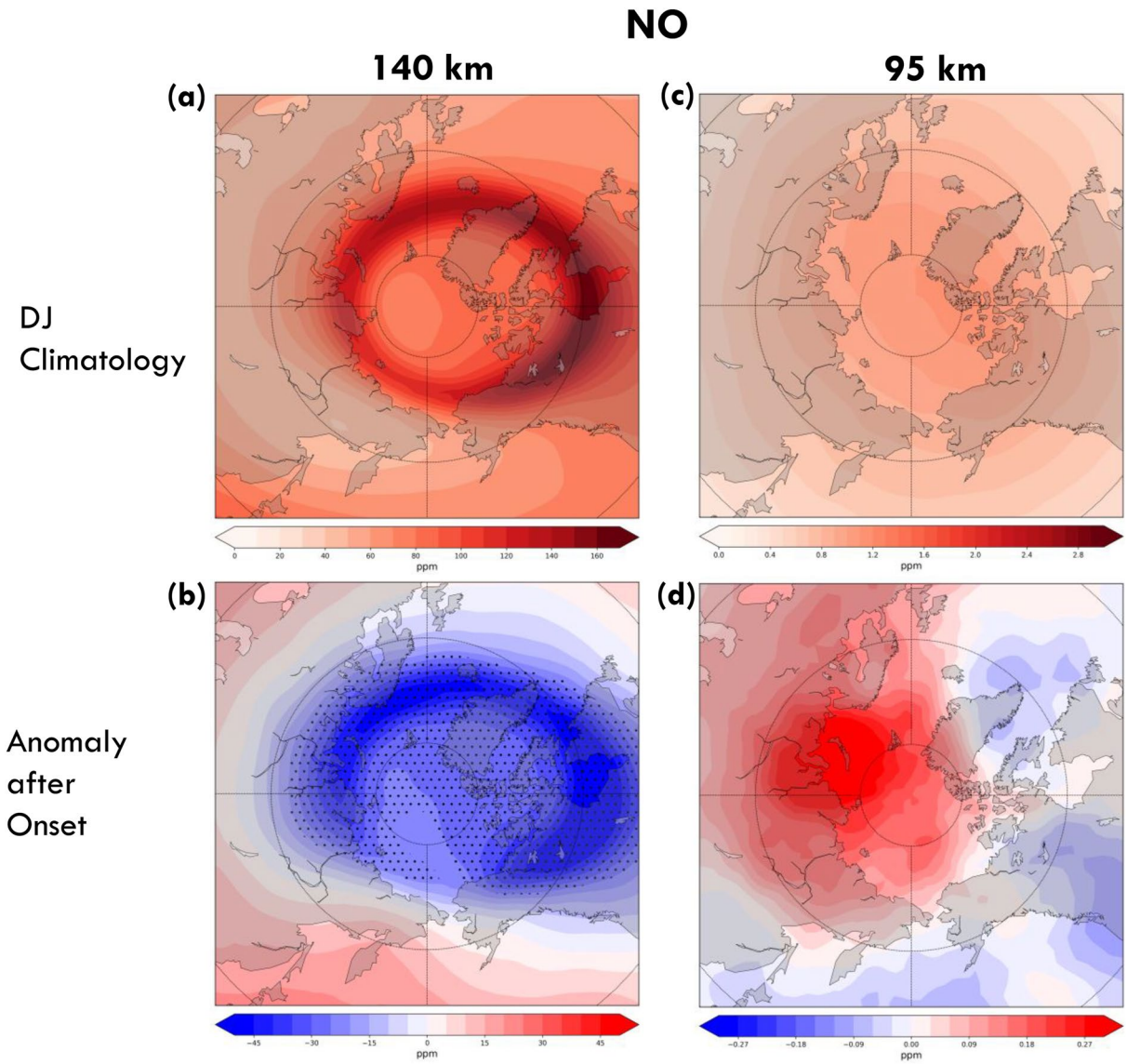

Figure 8. *Polar maps of NO*. Maps of the climatological NO at 140 and 95 km (a and c). The climatology is based on December and January, excluding ES-SSW events. Composite anomalies from 9 ES-SSW events and averaged over days [5, 15] after onset at the same altitudes are shown in panels (b and d). The units are ppm. Note the different color scales at different altitudes.

The composited temperature anomaly in Figure 3a extends into the thermosphere. In that region, background temperatures are strongly influenced by the 11-year solar cycle, changing by several hundred degrees between solar maximum and solar minimum. The inter-annual variations of zonal-mean temperatures averaged between 150 and 175 km and between 30 and 90°N are shown in Figure 10. A 2-month time average has been performed, December–January during quiet winters, else 1 month prior to 1 month following the onset for the winters with ES-SSWs. The solar radio flux (F10.7) is also shown, averaged over the same time period. We see that the majority of the 9 ES-SSWs (red bars) in our study occurs during relatively high phases of solar cycles 23 and 24, while the quiet winters (blue bars) were predominantly during low phases. Hence, the composite temperature anomaly with respect to the quiet winter climatology denotes a warming in this altitude range (Figure 3a). Our point is not to relate a dependency of the occurrences of ES-SSW to a particular phase of the solar cycle. Rather, it is merely to show that the sampled events -as it so happens- is biased toward events that occurred during high solar phase. Therefore, the background thermospheric temperature anomaly is hot (positive), as expected. On the contrary, the well-studied 2009 ES-SSW event occurred during solar minimum condition (Figure 10) and featured a lower thermospheric cooling anomaly (Goncharenko et al., 2021; Liu et al., 2014).

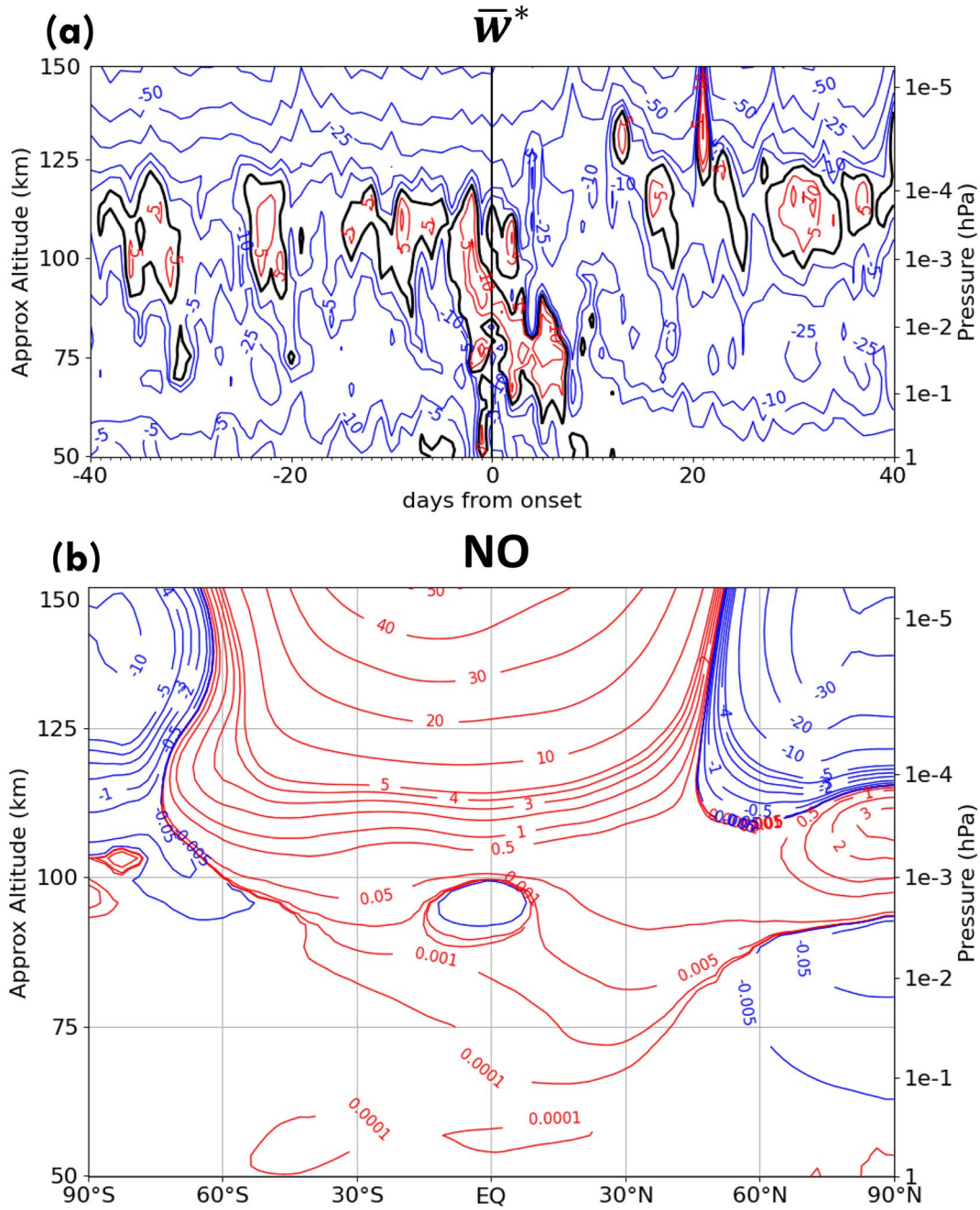

Figure 9. *The 2012/2013 ES-SSW*. Altitude-time cross-section of the vertical component of the residual mean meridional circulation. (a) A latitude averaging over 62–79°N was done. Red contours show the positive velocities, blue contours show the negative velocities, and the thick black contours indicate zero velocity. The unit is mm/s. (b) Altitude-meridional cross-section of the zonal-mean anomalies of NO mixing ratio and averaged over days [5, 15] after onset with red contours being positive anomalies and blue contours negative anomalies. Labels are indicated on contours. The unit is ppm.

Biases in the wintertime zonal wind between SD-WACCM-X and SuperDARN radar observations near 95 km were documented in Zhang et al. (2021) and Harvey et al. (2021). Outside of the periods of ES-SSW events, the current version of SD-WACCM-X features westward winds while the radar observed weak westerlies, indicating that the GW-induced westward drag in the model might be too strong or applied at an altitude range that is too low. However, these biases are much smaller during ES-SSWs than they are in a climatological sense (Zhang et al., 2021), hence they are unlikely to affect the results presented here.

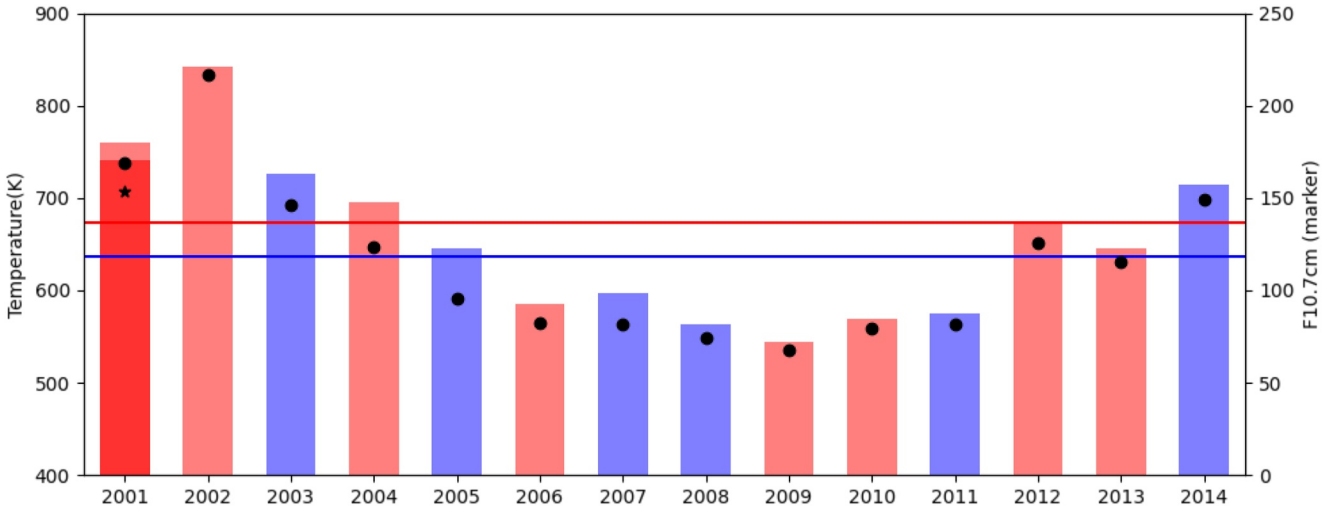

Figure 10. *Thermospheric temperatures*. Zonal-mean temperature averaged between 150 and 175 km for each individual year. The bar coloring indicates whether an ES-SSW event (or on one occasion two events) took place in the period or not. An average over a 2-month period was done, either December–January for quiet winters, else centered over the event. The F10.7 cm solar flux is also shown (black dot or star). A latitude averaging over 30–90°N was done.

In conclusion, we used existing simulations with WACCM-X in specified dynamics configuration to determine the respective roles of PWs, GWs, and tides in driving LT MMC, both climatologically and following ES-SSW onset. The main results are:

1. The northern hemisphere climatological LT MMC is driven by eastward-propagating GWs and extents vertically from approximately 100–125 km, as can be seen from the tightening of the CO_2 isopleths.
2. The LT MMC reverses briefly following ES-SSW onset, resulting in a "chimney-like" feature of un-interrupted polar descent from the altitude of 150 km down to the upper mesosphere.
3. The LT MMC reversal is driven by the WPW forcing, which exerts a brief but significant westward forcing, surpassing the parametrized GWD and providing the main contribution to the velocity streamfunction reversal at 110 km. The tidal forcings become important above 120 km.
4. The attendant descent leads to a short-lived enhancement of NO into the polar LT and upper mesosphere, in excess of 1 ppm at 110 km.

Since the climatological LT MMC is driven by GWs, whose parametrization is model-dependent, further detailed observation-based studies should be pursued to further constrain its characteristics and its subseasonal variability, and validate the aforementioned conclusions based on these WACCM-X simulations.

Appendix A: Decomposition of the GWD

The gravity wave (GW) drag (GWD) as archived in the SD-Whole-Atmosphere Community Climate Model (WACCM)-X simulations does not specify the contributions of GWs of different zonal phase speeds. Nevertheless, the importance of fast eastward GWs in driving the climatological lower thermosphere mean meridional circulation (LT MMC) in the northern hemisphere can be gauged by an analogy with from the SD-WACCM output. In simulations with SD-WACCM described in Limpasuvan et al. (2016), the specific contributions from the five categories of GW phase speeds were stored (with boundaries at ± 15 and ± 40 ms^{-1}). Figure A1 shows the total GWD comprising the contributions from the topographic, convective and frontal GWs (Figure A1a), as well as the contributions from frontal GWs of different phase speed ranges (Figures A1b–A1f), as latitudinal height cross-sections. A time average has been performed over December–January during quiet winters. Above 100 km, it is eastward over a broad range of latitudes. The fastest eastward-propagating GWs with phase speeds higher than +40 ms^{-1} provide the largest and, in fact, the only eastward contribution (Figures A1b–A1f). There are differences between SD-WACCM-X and SD-WACCM in their respective GW parametrization including in the allowed range of phase speeds, but the suggestion of Qian et al. (2017) that the forcing by fast eastward GWs drives the LT MMC in the northern hemisphere is supported by the SD-WACCM results in Figure A1. These parent models are driven by the same large-scale reanalyzes up to the stratopause layer, making it plausible that the fastest eastward-propagating GWs play a similar role in both models.

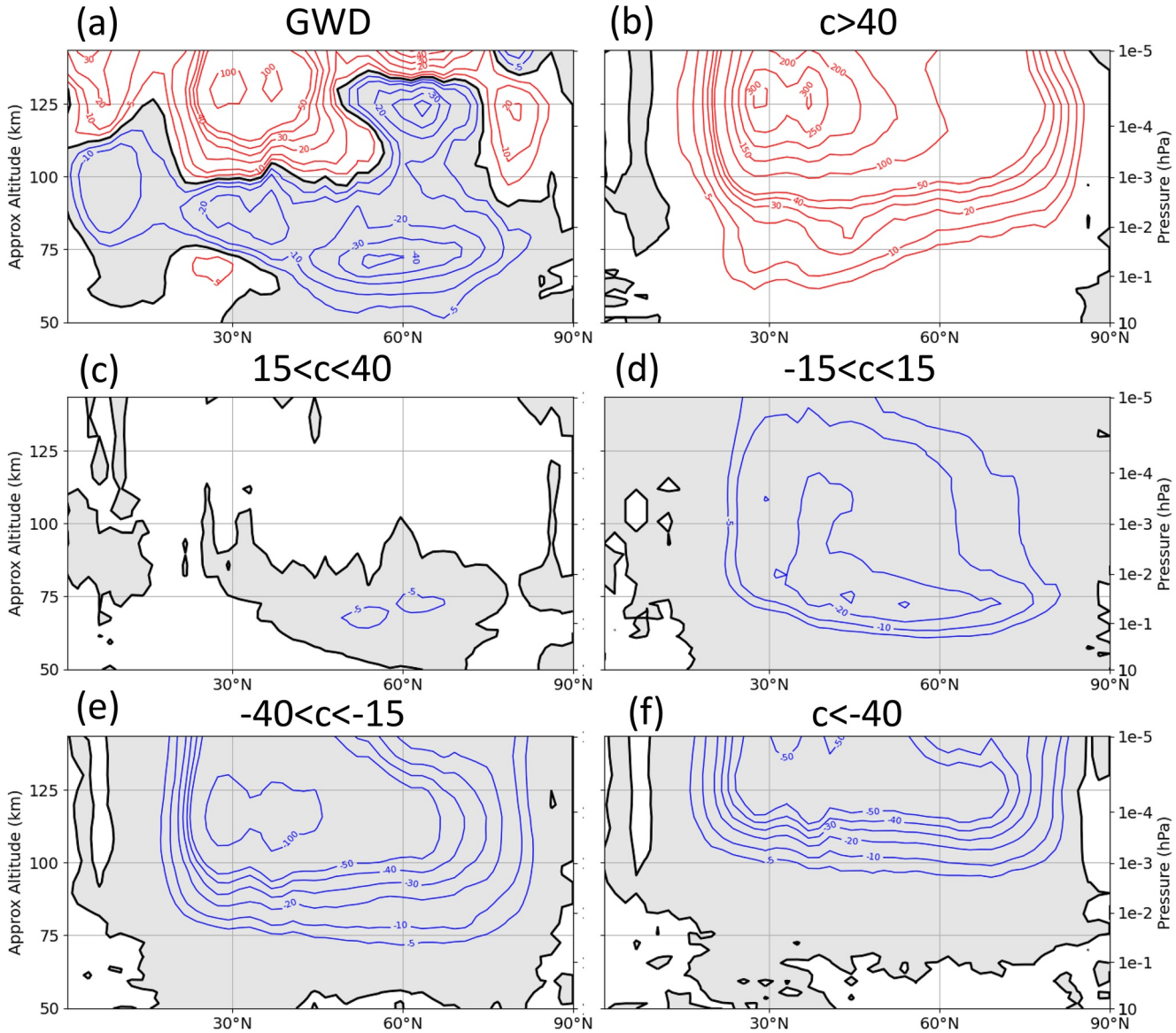

Figure A1. *Wintertime climatological components of zonal-mean wave forcing from frontal gravity waves* (*GWs*) *for SD-Whole-Atmosphere Community Climate Model*. Contributions from different classes frontal GW zonal phase speeds (b–f) and total frontal GW forcing (a). The climatology is based on December and January, in quiet winters without ES-SSW events. Red or blue contours indicate eastward or westward forcing respectively.

Data Availability Statement

The CESM2.0 SD-WACCM-X hourly data was accessed through Earth System Grid (https://www.earthsystemgrid.org), called CESM run f. e20. FXSD.f19_19.001 data. The extended SD-WACCM runs used in the Appendix A (Rhodes et al., 2021) are available at http://mirror.coastal.edu/sce/waccmsd1979_2015_var/.

Acknowledgments
JZ is supported by funding from NSF Awards (RUI AGS-1642232 and MRI AGS-1624068). We also acknowledge NCAR CISL computing support. VL is supported by NSF Intergovernmental Agreement.

References

Andrews, D. G., Holton, J. R., & Leovy, C. B. (1987). *Middle atmosphere dynamics* (p. 489). Academic Press.

Chandran, A., Collins, R. L., & Harvey, V. L. (2014). Stratosphere-mesosphere coupling during stratospheric sudden warming events. *Advances in Space Research*, *53*(9), 1265–1289. https://doi.org/10.1016/j.asr.2014.02.005

Chandran, A., Garcia, R. R., Collins, R. L., & Chang, L. C. (2013). Secondary planetary waves in the middle and upper atmosphere following the stratospheric sudden warming event of January 2012. *Geophysical Research Letters*, *40*(9), 1861–1867. https://doi.org/10.1002/grl.50373

Conte, J. F., Chau, J. L., & Peters, D. H. W. (2019). Middle- and high-latitude mesosphere and lower thermosphere mean winds and tides in response to strong polar-night jet oscillations. *Journal of Geophysical Research: Atmospheres*, *124*(16), 9262–9276. https://doi.org/10.1029/2019JD030828

Damiani, A., Funke, B., López Puertas, M., Gardini, A., von Clarmann, T., Santee, M. L., et al. (2014). Changes in the composition of the northern polar upper stratosphere in February 2009 after a sudden stratospheric warming. *Journal of Geophysical Research: Atmospheres*, *119*(19), 11429–11444. https://doi.org/10.1002/2014JD021698

Forbes, J. (2007). Dynamics of the thermosphere. *Journal of the Meteorological Society of Japan*, *85B*, 193–213. https://doi.org/10.2151/jmsj.85b.193

Funke, B., López-Puertas, M., Bermejo-Pantaleón, D., García-Comas, M., Stiller, G. P., von Clarmann, T., et al. (2010). Evidence for dynamical coupling from the lower atmosphere to the thermosphere during a major stratospheric warming. *Geophysical Research Letters*, *37*(13), L13803. https://doi.org/10.1029/2010GL043619

Garcia, R. R., Lopez-Puertas, M., Funke, B., Marsh, D. R., Kinnison, D. E., Smith, A. K., & Gonzalez-Galindo, F. (2014). On the distribution of CO_2 and CO in the mesosphere and lower thermosphere. *Journal of Geophysical Research: Space*, *119*(9), 5700–5718. https://doi.org/10.1002/2013jd021208

García-Comas, M., Funke, B., López-Puertas, M., González-Galindo, F., Kiefer, M., & Höpfner, M. (2020). First detection of a brief mesoscale elevated stratopause in very early winter. *Geophysical Research Letters*, *47*(4), e2019GL086751. https://doi.org/10.1029/2019GL086751

Gelaro, R., McCarty, W., Suárez, M. J., Todling, R., Molod, A., Takacs, L., et al. (2017). The modern-era retrospective analysis for research and applications, version 2 (MERRA-2). *Journal of Climate*, *30*(14), 5419–5454. https://doi.org/10.1175/JCLI-D-16-0758.1

Goncharenko, L. P., Coster, A. J., Plumb, R. A., & Domeisen, D. I. V. (2012). The potential role of stratospheric ozone in the stratosphere-ionosphere coupling during stratospheric warmings. *Geophysical Research Letters*, *39*(8), L08101. https://doi.org/10.1029/2012GL051261

Goncharenko, L. P., Harvey, L., Liu, H., & Pedatella, N. M. (2021). Sudden stratospheric warming impacts on the ionosphere-thermosphere system: A review of recent progress. In *Advances in ionospheric research: Current understanding and challenges*. American Geophysical Union.

Harvey, V. L., Datta-Barua, S., Pedatella, N. M., Wang, N., Randall, C. E., Siskind, D. E., & van Caspel, W. E. (2021). Transport of nitric oxide via Lagrangian coherent structures into the top of the polar vortex. *Journal of Geophysical Research: Atmospheres*, *126*(11), e2020JD034523. https://doi.org/10.1029/2020JD034523

Hibbins, R., Espy, P. J., Orsolini, Y., Limpasuvan, V., & Barnes, R. J. (2019). SuperDARN observations of semidiurnal tidal variability in the MLT and the response to sudden stratospheric warming events. *Journal of Geophysical Research: Atmospheres*, *124*(9), 4862–4872. https://doi.org/10.1029/2018jd030157

Holt, L. A., Randall, C. E., Peck, E. D., Marsh, D. R., Smith, A. K., & Harvey, V. L. (2013). The influence of major sudden stratospheric warming and elevated stratopause events on the effects of energetic particle precipitation in WACCM. *Journal of Geophysical Research: Atmospheres*, *118*(20), 11636–11646. https://doi.org/10.1002/2013JD020294

Iida, C., Hirooka, T., & Eguchi, N. (2014). Circulation changes in the stratosphere and mesosphere during the stratospheric sudden warming event in January 2009. *Journal of Geophysical Research: Atmospheres*, *119*(12), 7104–7115. https://doi.org/10.1002/2013JD021252

Iwao, K., & Hirooka, T. (2021). Opposite contributions of stationary and traveling planetary waves in the northern hemisphere winter middle atmosphere. *Journal of Geophysical Research: Atmospheres*, *126*(9), e2020JD034195. https://doi.org/10.1029/2020JD034195

Jin, H., Miyoshi, Y., Pancheva, D., Mukhtarov, P., Fujiwara, H., & Shinagawa, H. (2012). Response of migrating tides to the stratospheric sudden warming in 2009 and their effects on the ionosphere studied by a whole atmosphere-ionosphere model GAIA with COSMIC and TIMED/SABER observations. *Journal of Geophysical Research*, *117*(A10), A10323. https://doi.org/10.1029/2012JA017650

Jones, M., Jr., Siskind, D. E., Drob, D. P., McCormack, J. P., Emmert, J. T., Dhadly, M. S., et al. (2020). Coupling from the middle atmosphere to the exobase: Dynamical disturbance effects on light chemical species. *Journal of Geophysical Research: Space*, *125*(10), e2020JA028331. https://doi.org/10.1029/2020JA028331

Laskar, F. I., McCormack, J. P., Chau, J. L., Pallamraju, D., Hoffmann, P., & Singh, R. P. (2019). Interhemispheric meridional circulation during sudden stratospheric warming. *Journal of Geophysical Research: Space*, *124*(8), 7112–7122. https://doi.org/10.1029/2018JA026424

Limpasuvan, V., Orsolini, Y. J., Chandran, A., Garcia, R. R., & Smith, A. K. (2016). On the composite response of the MLT to major sudden stratospheric warming events with elevated stratopause. *Journal of Geophysical Research: Atmospheres*, *121*(9), 4518–4537. https://doi.org/10.1002/2015jd024401

Limpasuvan, V., Richter, J. H., Orsolini, Y. J., Stordal, F., & Kvissel, O.-K. (2012). The roles of planetary and gravity waves during a major stratospheric sudden warming as characterized by WACCM. *Journal of Atmospheric and Solar-Terrestrial Physics*, *78–79*, 84–98. https://doi.org/10.1016/j.jastp.2011.03.004

Liu, H., Miyoshi, Y., Miyahara, S., Jin, H., Fujiwara, H., & Shinagawa, H. (2014). Thermal and dynamical changes of the zonal mean state of the thermosphere during the 2009 SSW: GAIA simulations. *Journal of Geophysical Research: Space*, *119*(8), 6784–6791. https://doi.org/10.1002/2014JA020222

Liu, H.-L. (2007). On the large wind shear and fast meridional transport above the mesopause. *Geophysical Research Letters*, *34*(8), L08815. https://doi.org/10.1029/2006GL028789

Liu, H.-L., Bardeen, C. G., Foster, B. T., Lauritzen, P., Liu, J., Lu, G., et al. (2018). Development and validation of the whole atmosphere community climate model with thermosphere and ionosphere extension (WACCM-X). *Journal of Advances in Modeling Earth Systems*, *10*(2), 381–402. https://doi.org/10.1002/2017MS001232

Lossow, S., Urban, J., Schmidt, H., Marsh, D. R., Gumbel, J., Eriksson, P., & Murtagh, D. (2009). Wintertime water vapour in the polar upper mesosphere and lower thermosphere – First satellite observations by Odin submillimeter radiometer. *Journal of Geophysical Research*, *114*(D10), D10304. https://doi.org/10.1029/2008jd011462

Manney, G. L., Kruger, K., Pawson, S., Minschwaner, K., Schwartz, M. J., Daffer, W. H., et al. (2008). The evolution of the stratopause during the 2006 major warming: Data and assimilated meteorological analyses. *Journal of Geophysical Research*, *113*(D11), D11115. https://doi.org/10.1029/2007jd009097

Manney, G. L., Schwartz, M. J., Kruger, K., Santee, M. L., Pawson, S., Lee, J. N., et al. (2009). Aura Microwave Limb Sounder observations of dynamics and transport during the record-breaking 2009 Arctic stratospheric major warming. *Geophysical Research Letters*, *36*(12), L12815. https://doi.org/10.1029/2009gl038586

Marsh, D. R., Mills, M. J., Kinnison, D. E., Lamarque, J.-F., Calvo, N., & Polvani, L. M. (2013). Climate change from 1850 to 2005 simulated in CESM1(WACCM). *Journal of Climate*, *26*(19), 7372–7391. https://doi.org/10.1175/JCLI-D-12-00558.1

McInerney, J. M., Marsh, D. R., Liu, H.-L., Solomon, S. C., Conley, A. J., & Drob, D. P. (2018). Simulation of the August 21, 2017 solar eclipse using the whole atmosphere community climate model-eXtended. *Geophysical Research Letters*, *45*(9), 3793–3800. https://doi.org/10.1029/2018GL077723

Miyoshi, Y., Fujiwara, H., Jin, H., & Shinagawa, H. (2015). Impacts of sudden stratospheric warming on general circulation of the thermosphere. *Journal of Geophysical Research: Space*, *120*(12), 10897–10912. https://doi.org/10.1002/2015JA021894

Oberheide, J., Pedatella, N. M., Gan, Q., Kumari, K., Burns, A. G., & Eastes, R. (2020). Thermospheric composition O/N_2 response to an altered meridional mean circulation during sudden stratospheric warmings observed by GOLD. *Geophysical Research Letters*, *47*(1), e2019GL086313. https://doi.org/10.1029/2019GL086313

Oberländer, S., Langematz, U., & Meul, S. (2013). Unraveling impact factors for future changes in the Brewer-Dobson circulation. *Journal of Geophysical Research: Atmospheres*, *118*(18), 10296–10312. https://doi.org/10.1002/jgrd.50775

Okui, H., Sato, K., Koshin, D., & Watanabe, S. (2021). Formation of a mesospheric inversion layer and the subsequent elevated stratopause associated with the major stratospheric sudden warming in 2018/19. *Journal of Geophysical Research: Atmospheres*, *126*(18), e2021JD034681. https://doi.org/10.1029/2021JD034681

Orsolini, Y. J., Limpasuvan, V., Pérot, K., Espy, P. J., Hibbins, R., Lossow, S., et al. (2017). Modelling the descent of NO during the elevated stratopause event of January 2013. *Journal of Atmospheric and Solar-Terrestrial Physics*, *155*, 50–61. https://doi.org/10.1016/j.jastp.2017.01.006

Orsolini, Y. J., Urban, J., Murtagh, D. P., Lossow, S., & Limpasuvan, V. (2010). Descent from the polar mesosphere and anomalously high stratopause observed in 8 years of water vapor and temperature satellite observations by the Odin Sub-Millimeter Radiometer. *Journal of Geophysical Research*, *115*(D12), D12305. https://doi.org/10.1029/2009jd013501

Pedatella, N. M., Fuller-Rowell, T., Wang, H., Jin, H., Miyoshi, Y., Fujiwara, H., et al. (2014). The neutral dynamics during the 2009 sudden stratosphere warming simulated by different whole atmosphere models. *Journal of Geophysical Research: Space*, *119*(2), 1306–1324. https://doi.org/10.1002/2013JA019421

Pérot, K., & Orsolini, Y. J. (2021). Impact of the major SSWs of February 2018 and January 2019 on the middle atmospheric nitric oxide abundance. *Journal of Atmospheric and Solar-Terrestrial Physics*, *218*, 105586. https://doi.org/10.1016/j.jastp.2021.105586

Qian, L., Burns, A., & Yue, J. (2017). Evidence of the lower thermospheric winter-to-summer circulation from SABER CO_2 observations. *Geophysical Research Letters*, *44*(20), 10100–10107. https://doi.org/10.1002/2017gl075643

Qian, L., & Yue, J. (2017). Impact of the lower thermospheric winter-to-summer residual circulation on thermospheric composition. *Geophysical Research Letters*, *44*(9), 3971–3979. https://doi.org/10.1002/2017gl073361

Rhodes, C. T., Limpasuvan, V., & Orsolini, Y. J. (2021). Eastward-propagating planetary waves prior to the January 2009 sudden stratospheric warming. *Journal of Geophysical Research: Atmospheres*, *126*(11), e2020JD033696. https://doi.org/10.1029/2020JD033696

Sassi, F., Liu, H.-L., Ma, J., & Garcia, R. R. (2013). The lower thermosphere during the northern hemisphere winter of 2009: A modeling study using high-altitude data assimilation products in WACCM-X. *Journal of Geophysical Research: Atmospheres*, *118*(16), 8954–8968. https://doi.org/10.1002/jgrd.50632

Sassi, F., McCormack, J. P., Tate, J. L., Kuhl, D. D., & Baker, N. L. (2021). Assessing the impact of middle atmosphere observations on day-to-day variability in lower thermospheric winds using WACCM-X. *Journal of Atmospheric and Solar-Terrestrial Physics*, *212*, 105486. https://doi.org/10.1016/j.jastp.2020.105486

Sato, K., & Hirano, S. (2019). The climatology of the Brewer–Dobson circulation and the contribution of gravity waves. *Atmospheric Chemistry and Physics*, *19*(7), 4517–4539. https://doi.org/10.5194/acp-19-4517-2019

Siskind, D. E., Harvey, V. L., Sassi, F., McCormack, J. P., Randall, C. E., Hervig, M. E., & Bailey, S. M. (2021). Two- and three-dimensional structure of the descent of mesospheric trace constituents after the 2013 SSW elevated stratopause event. *Atmospheric Chemistry and Physics*, *21*(18), 14059–14077. https://doi.org/10.5194/acp-21-14059-2021

Siskind, D. E., Sassi, F., Randall, C. E., Harvey, V. L., Hervig, M. E., & Bailey, S. M. (2015). Is a high-altitude meteorological analysis necessary to simulate thermosphere-stratosphere coupling? *Geophysical Research Letters*, *42*(19), 8225–8230. https://doi.org/10.1002/2015GL065838

Smith, A. K., Garcia, R. R., Marsh, D. R., & Richter, J. H. (2011). WACCM simulations of the mean circulation and trace species transport in the winter mesosphere. *Journal of Geophysical Research*, *116*(D20), D20115. https://doi.org/10.1029/2011JD016083

Smith, A. K., Lopez-Puertas, M., Garcia-Comas, M., & Tukiainen, S. (2009). SABER observations of mesospheric ozone during NH late winter 2002–2009. *Geophysical Research Letters*, *36*(23), L23804. https://doi.org/10.1029/2009gl040942

Solomon, S. C., Liu, H.-L., Marsh, D. R., McInerney, J. M., Qian, L., & Vitt, F. M. (2018). Whole atmosphere simulation of anthropogenic climate change. *Geophysical Research Letters*, *45*(3), 1567–1576. https://doi.org/10.1002/2017GL076950

Stray, N. H., Orsolini, Y. J., Espy, P. J., Limpasuvan, V., & Hibbins, R. E. (2015). Observations of planetary waves in the mesosphere-lower thermosphere during stratospheric warming events. *Atmospheric Chemistry and Physics*, *15*(9), 4997–5005. https://doi.org/10.5194/acp-15-4997-2015

Tomikawa, Y., Sato, K., Watanabe, S., Kawatani, Y., Miyazaki, K., & Takahashi, M. (2012). Growth of planetary waves and the formation of an elevated stratopause after a major stratospheric sudden warming in a T213L256 GCM. *Journal of Geophysical Research*, *117*(D16), D16101. https://doi.org/10.1029/2011JD017243

Tweedy, O. V., Limpasuvan, V., Orsolini, Y. J., Smith, A. K., Garcia, R., Randall, C., et al. (2013). Nighttime secondary ozone layer during major stratospheric sudden warmings in specified-dynamics WACCM. *Journal of Geophysical Research: Atmospheres*, *118*(15), 8346–8358. https://doi.org/10.1002/jgrd.50651

Wang, N., Qian, L., Yue, J., Wang, W., Mlynczak, M. G., & Russell, J. M., III. (2022). Climatology of mesosphere and lower thermosphere residual circulations and mesopause height derived from SABER observations. *Journal of Geophysical Research: Atmospheres*, *127*(4), e2021JD035666. https://doi.org/10.1029/2021JD035666

Yue, J., & Wang, W. (2014). Changes of thermospheric composition and ionospheric density caused by quasi 2 day wave dissipation. *Journal of Geophysical Research: Space Physics*, *119*(3), 2069–2078. https://doi.org/10.1002/2013JA019725

Zhang, J., Limpasuvan, V., Orsolini, Y. J., Espy, P. J., & Hibbins, R. E. (2021). Climatological westward-propagating semidiurnal tides and their composite response to sudden stratospheric warmings in SuperDARN and SD-WACCM-X. *Journal of Geophysical Research: Atmospheres*, *126*(3), e2020JD032895. https://doi.org/10.1029/2020JD032895